Understanding and Benchmarking Ground Reflectors for Bifacial Photovoltaic Yield Enhancement

Shweta S Pal, Frank H C van Loenhout, Jelle Westerhof, and Rebecca Saive

***Abstract*—Bifacial modules combined with optimally positioned ground reflectors (albedo) can boost photovoltaic (PV) yield. Yet, a rigorous understanding and benchmarking of the reflector performance is missing, which leads to errors in power yield and economic estimates, thus hampering PV market penetration. Here, we address this impediment by establishing an experimentally validated reverse ray tracing (RRT) approach, combined with empirically derived parameters. First, we determine the spectro-angular reflection of a wide class of ground reflectors (diffuse, glossy, and specular). These parameters were fed into our RRT software, that simulated the PV yield, which was then experimentally validated with a model PV system. The validated framework enables determining an upper limit to PV yield enhancement and current mismatch within modules exposed to different kinds of reflectors. Our approach helps assessing already-existing natural and exotic reflectors, and inspire novel reflectors for enhanced PV yield and economic benefits.**

***Index Terms*—Albedo, bifacial solar, optical modeling, reflectors, reverse ray tracing.**

I. Introduction

MARKET penetration of an energy source is primarily driven by the levelized cost of electricity (LCOE), i.e., the ratio of the total cost incurred by a power plant to the total energy generated over its lifetime. Photovoltaic (PV) solar panels have become one of the most cost-effective ways to generate energy sustainably and recent studies show that installing new solar plants is already less expensive than operating existing coal power plants [1]. Nonetheless, their LCOE needs to further decrease for solar to become a clear favorite in most countries and thereby accelerate the transition to a 100% renewable future. To minimize the LCOE, the PV yield must be increased, while keeping the costs low. A lucrative candidate to achieve this are bifacial modules. These panels accept light from both faces, i.e., the front and the rear, as opposed to their conventional monofacial counterparts, thereby allowing for capturing diffuse and ground reflected (albedo) light. Furthermore, bifacial modules enable novel types of solar integration such as vertical installations in combination with agriculture [2], [3], [4], [5]. As a consequence, the International Technological Roadmap of Photovoltaic 2021, predicts an increase for world bifacial market share from 48% in 2021 to 78% in 2031 [6].

Nevertheless, the bifacial market is facing the major problem, that the LCOE is difficult to predict as the ground reflectance, i.e., albedo, strongly influences the yield [7], [8]. Understanding and optimizing the influence of albedo for accurate LCOE predictions and enhanced yield is crucial to establish an even stronger solar advantage. The spectral [9], [10], [11] and angular reflectance of the ground must be carefully taken into account as PV power generation depends on the spectrum [12], [13] and angle of incidence [14] of the irradiance reaching the module. Generally, ground reflectors are assessed by their angle and/or wavelength-averaged albedo [7], [15], [16], [17], [18], [19]. This can lead to errors in power and LCOE estimation of up to 23.6% and 65.2%, respectively [20]. Therefore, a computational and experimental framework to assess the spectro-angular albedo-dependent yield of a module is proposed here. The software readily allows for accommodating any incoming illumination and intricate spectral and angular dependance of natural (paint, grass, concrete, and gravel) and exotic (metamaterials [21], free space luminescent solar concentrators [22], [23], and holographic reflectors [24]) reflectors. Using this methodology in conjunction with an optimization algorithm, one can even design new classes of artificial reflectors. The aforementioned methodology can enable accurate LCOE predictions and a more extensive search and benchmarking of albedo materials, which could outperform naturally occurring surfaces. These could be designed for maximum annual yield, maximum performance during high-energy demand times, robustness to the solar path, economic feasibility of solar-tracking, mismatch, or losses due to spatially inhomogeneous illumination introduced by the reflector. This comprehensive approach allows for a fundamental way of discussing and improving the surface properties of a reflector to investigate albedo-dependent PV output more reliably.

Manuscript received 20 July 2023; revised 8 September 2023; accepted 23 September 2023. This work was supported by the University of Twente Faculty of Science and Technology Tenure Track Start-up Package. *(Corresponding author: Rebecca Saive.)*

The authors are with the MESA+ Institute for Nanotechnology, University of Twente, 7522 Enschede, The Netherlands (e-mail: s.s.pal@utwente.nl; f.h.c.vanloenhout@student.utwente.nl; j.westerhof@student.utwente.nl; r.saive@utwente.nl).

Color versions of one or more figures in this article are available at https://doi.org/10.1109/JPHOTOV.2023.3319592.

Digital Object Identifier 10.1109/JPHOTOV.2023.3319592

II. Quantifying Albedo-Dependent Yield

The hypothesis at the core for describing any albedo is that the total reflection function can be given as a linear combination of reflection functions, with the three main functions being specular, glossy, and diffuse [schematic shown in Fig. 1(a)–(c)]. This concept was first introduced in 1965 [25] and is commonly referred to as bidirectional reflectance distribution function (BRDF). Various variations of BRDFs have been proposed,

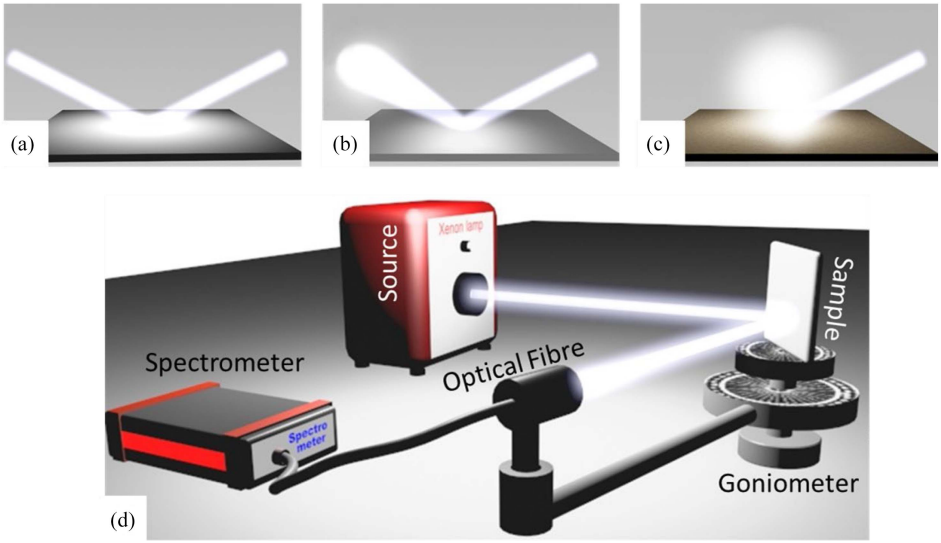

Fig. 1. Schematic of a (a) diffuse, (b) glossy, and (c) specular reflector (light incident from the right), and (d) the goniometer for spectro-angular reflection measurements. The set-up consists of a white light source for illumination, a sample holder on a tilt stage to control the angle of incidence, and a fiber-couple spectrometer on a different tilt stage to independently control the viewing angle.

whereas we use the following definitions to comply with the laws of physics as detailed in [20]. Mathematically, the total reflection function R_T $[sr^{-1}]$ is then given as

$$R_T = k_S\, R_S + k_G R_G + k_D R_D \tag{1}$$

$$\text{such that,} \qquad k_S + k_G + k_D \leq 1 \tag{2}$$

$$R_S = \frac{\delta\left(\theta - \theta_r\right)\delta\left(\phi - \phi_r\right)}{\cos\theta_r} \tag{3}$$

$$R_G = GGX\left(\theta_i,\ \phi_i, \theta,\ \phi,\ m, n, k, \lambda\right) \tag{4}$$

$$R_D = \frac{1}{\pi} \tag{5}$$

where R_S, R_G, and R_D represent the spectral and angular reflection function of a specular, glossy, and diffuse reflector, respectively. k_S, k_G, and k_D denote the fraction of energy that is specular, glossy, or diffuse in nature, respectively. For clarity, a completely diffusive material will have $k_D = 1$, whereas a completely specular material will have $k_S = 1$. These coefficients are determined experimentally using a goniometer explained in the following section. λ is the wavelength of the incoming irradiance, and θ and ϕ are the zenith and azimuth angles, respectively, according to the spherical coordinate system. $\delta(x - x_0)$ is the Dirac delta distribution, the subscripts *i* and *r* denote the direction of the incidence and reflection. To emulate a glossy surface, we choose the GGX theory for its physics-based approach [26]. It requires surface roughness, refractive index, and absorption coefficient as input parameters and calculates the glossy (reflection) lobe. Throughout the entire investigation, we assume azimuthal symmetry. In this work, the bifacial output due to a generic aluminium mirror, a generic white paper, and a generic photopaper as reflectors is simulated, and then experimentally validated. The aforementioned materials were used as they exhibit the classic cases of specular, diffuse and glossy reflectors, and allow for robust and reproducible experimental results. First, the spectro-angular albedo of the reflector is accurately characterized in terms of $[\mathrm{k_S}, \mathrm{k_G}, \mathrm{k_D}]$, which are determined using a goniometer. By combining the experimentally obtained k coefficients and $\mathrm{R_T}$ into the reverse ray-tracing software, in accordance with (1)–(5), the bifacial photovoltaic output due to a mirror, paper, and photopaper is computed. The technical details of the three-dimensional (3-D) reverse ray-tracing software can be found in [20]. Finally, the albedo-dependent bifacial output was measured. An excellent agreement between the proposed framework and the experimental data was found as will be shown below.

III. κ_S, k_G, k_D Measurements

Determining the nature of a material using k coefficients requires spectral and angular reflectance measurements over the entire upper hemisphere of the sample. For this, a compact goniometer [see Fig. 1(d)] was designed. The experimental set-up consists of a white light source (Thorlabs SLS401), a sample holder, and a fiber-coupled spectrometer. The sample holder is situated on a rotation stage so that the angle of incidence can be varied. The optical fiber was attached to a rotating arm so that the viewing angle can be independently varied and data can be recorded for a fixed azimuth angle but various zenith angles. The sample can be rotated about its own normal to change the azimuth angle. The three samples investigated were: 1) a generic mirror (specular reflector) (11 cm $\times$ 14.2 cm); 2) a generic A4 photopaper (glossy reflector); and 3) a generic A4 paper (diffuse reflector). Here, as a reference, a paper coated with spectralon [27] (measured reflectance $= 98\%$) was used. Spectralon is a fluoro-polymer paint, which has the highest diffuse reflectance known so far [28].

A. Angular Reflectance Using a Goniometer

The measured angular reflectance of spectralon, paper, photopaper, and mirror at $\lambda = 600$ nm for various angle of incidences can be seen in Fig. 2(a)–(d), respectively. For all the samples, it is to be noted that the data points are missing when

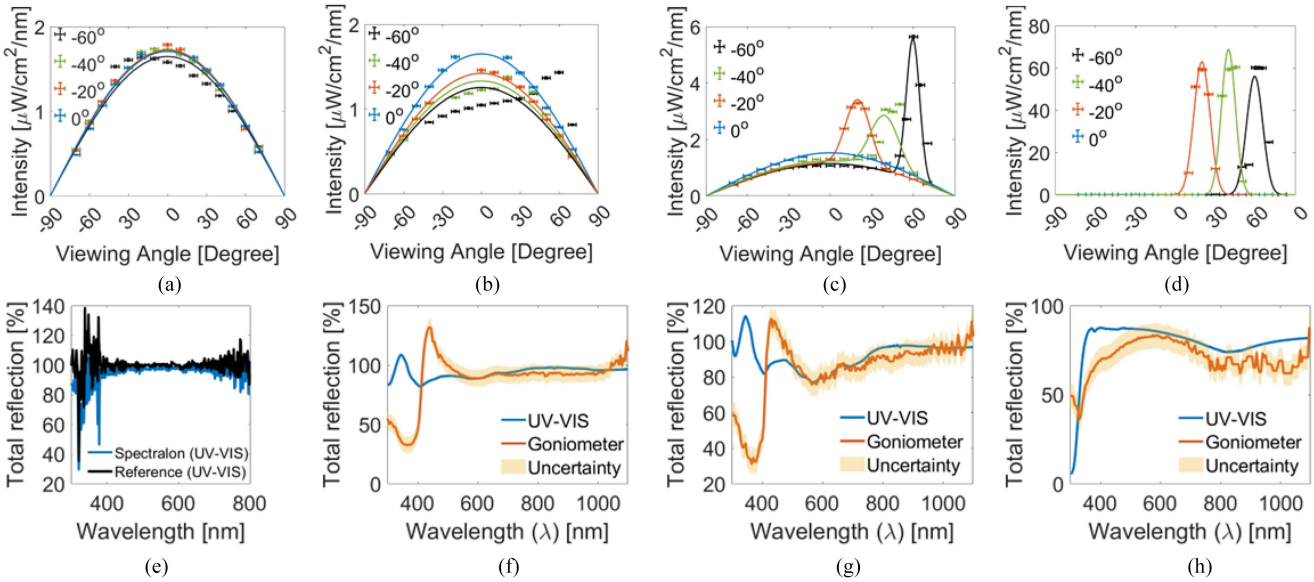

Fig. 2. (a)–(d) Angular reflectance of (a) spectralon, (b) paper, (c) photopaper, and (d) mirror, respectively, at $\lambda = 600$ nm for various angles of incidences relative to the reflector's normal. (e) Spectral reflectance of our spectralon sample measured with a UV-VIS spectrophotometer relative to the UV-VIS spectralon reference. (f)–(g) Angle integrated spectral reflectance using a UV-VIS spectrophotometer with integrating sphere and by computationally integrating the goniometer results for (f) paper, (g) photopaper, and (h) mirror.

the viewing angle is equal to the angel of incidence (AoI). This is done to prevent the eclipsing of the source by the detector. For this reason, the sharp peaks for glossy and mirror reflectors at AoI $= 0^\circ$ are absent. For spectralon, we see the standard cosine behaviour as must be displayed by a diffuse reflector [see Fig. 2(a)]. Although, for AoI $= -60^\circ$, we see noncosine like behavior. This is because of retro-scattering due to uneven spectralon layers. Retro-scattering is the scattering of light in the direction it came from, i.e., direction of the source. For paper, in Fig. 2(b), we also see a cosine behavior indicating its diffusive nature, but the magnitude is lower than that of the spectralon. Also, for paper, we see deviation from the cosine curve for AoI $= -40^\circ$ and AoI $= -60^\circ$. This is due to the fact that at grazing angles the reflection tends to be more specular. For photopaper [see Fig. 2(c)], interestingly, we see a combination of diffuse and glossy nature shown by the cosine curve and sharp peaks for all the angle of incidences (except AoI $= 0^\circ$). Finally, for a mirror [see Fig. 2(d)], we only see sharp peaks, indicating specular, or highly glossy nature for all the angle of incidences. Overall, one must also note the difference in magnitude as we move from diffusive samples to specular samples.

B. Calculating the k Coefficients

The k coefficients are calculated relative to the spectralon-coated paper. For a given sample, at a given wavelength, the angular reflectance seen in Fig. 2(a)–(d) was first extrapolated for all the azimuth angles by assuming rotational symmetry around the angle with maximum reflection. This gives a 3-D reflectance curve. For a glossy sample, the diffuse curve and the glossy curve were extrapolated separately. The volume under the extrapolated 3-D curve was determined. Finally, this calculated volume for a given sample was divided by the volume of the spectralon-coated paper. The resulting ratio gives the k coefficients for a given sample. The final wavelength-averaged k coefficients for the three samples are shown in Table I.

TABLE I
κ COEFFICIENTS FOR THE SAMPLES

Sample	$[k_S, k_G, k_D]$
Paper	[0, 0, 0.82]
Photopaper	[0, 0.06, 0.68]
Mirror	[0.79,0,0]

C. Verifying the Goniometer Measurements

To verify the abovementioned experimental results, the spectro-angular reflectance data [see Fig. 2(a)–(d)] was used to calculate the total spectral reflectance of a sample, and then, compared to the total spectral reflectance measured with a UV-VIS spectrophotometer and an integrating sphere (Relative error of 1%) [29]. Total spectral reflectance is the angle-integrated spectrally-resolved reflectance. To obtain the calculated spectral total reflectance from the goniometer measurements, for a given wavelength, the angular reflectance was integrated over all the angles as explained previously. For the measured total spectral reflectance, a spectrophotometer was used. It consisted of a broadband light source for illumination, a monochromator for sweeping over wavelengths, a sample holder, an integrating sphere for collecting all reflected light, and a photodiode for detection. The beam emitted by the source passes through a monochromator first and is then split into two beams, one of which is used for illuminating the sample, and the other is used as reference for normalization. The reflected light is collected by

a spectralon coated integrating sphere. Since the light reflected by the sample is collected and diffused by the integrating sphere, the angular resolution is lost. The photodiode records the reflected intensity for each wavelength. This measured signal is then normalized. A sweep over the desired wavelength range gives the total spectral reflectance. To be concise, we mathematically integrate the goniometer measurements over the upper hemisphere to get the total spectral reflectance, whereas the UV-VIS spectrophotometer measures the angle-integrated spectral reflectance over the upper hemisphere experimentally.

We begin the discussion by first determining the quality of the spectralon-coated paper against the homogenously-coated spectralon reference of the UV-VIS spectrophotometer, using the measured total spectral reflectance [see Fig. 2(e)]. This step is important as the spectralon-coated paper was used as a reference for calculating the k-coefficients, and a high-quality must be ensured. We see that the total spectral reflectance of the spectralon-coated paper is nearly identical to that of the homogenously-coated UV-VIS spectralon reference. This assures us of the quality of the spectralon-coated paper.

The results for paper, photopaper, and mirror are shown in Fig. 2(e)–(h), respectively, for near-normal incidence (AoI $=$ 5°). For paper and photopaper [see Fig. 2(f) and (g)], we see the goniometer and UV-VIS measurements match well, except for the 400 nm $<\lambda<$ 450 nm. For 400 nm $<\lambda<$ 450 nm, the calculated total reflectance value goes beyond 1. This is because generic white paper and photopaper tend to have optical brightening agents (OBA) for enhancing whiteness [30]. OBA are chemicals that absorbs UV light ($\lambda <$ 400 nm) and emit longer wavelength, mainly blue. The spectrometer detects this downshift, thus leading to a reflectance greater than 1 as explained below. The signatures of OBA can be seen in UV-VIS measurements of the respective samples at $\lambda <$ 350 nm. For $\lambda <$ 350 nm, the UV-VIS total reflectance value for paper and photopaper is above 1. This is because a UV-VIS spectrophotometer measures the total spectral reflectance by illuminating the sample with one wavelength at a time and measuring the reflected signal using a photodiode calibrated for that given wavelength. Therefore, when the sample is illuminated with UV light, the down-converted wavelengths emitted by the OBAs are registered as the UV wavelengths. This is because the photodiode cannot distinguish the photons spectrally. Therefore, at the absorption wavelength (∼345 nm), it overcounts the photons as it using its spectral response for 345 nm instead of the one for 440 nm. However, the grating-based spectrometer can detect and assign the correct wavelengths, thus showing the signatures of the down-converted light at the correct wavelength, which leads to a reflectance value greater than 1 for the emitted wavelengths (∼440 nm) and a very low reflection for the absorbed wavelength (∼345 nm). Finally, for the mirror sample [see Fig. 2(h)], we again see that the goniometer and UV-VIS measurements match well. Further details of set-up and additional results can be found in [31].

The abovementioned results clearly demonstrate the robustness of k coefficients in accurately quantifying the spectral and angular reflectance of a given sample. Moreover, our compact goniometer does not only match the sophisticated and more expensive UV-VIS results, but also detects the reflected spectrum better.

IV. Experimental Verification

This section discusses the experimental verification of our framework. The simulated albedo-dependent short-circuit current density (J_{sc}) of a bifacial module, as a function of cell height (h) and cell tilt (t), are compared. We investigated the influence of the albedo surfaces characterised from the previous section, i.e., the same generic mirror, generic A4 photopaper, and generic A4 white paper. For the experiment, a set-up [see Fig. 3(a)] was designed, which consists of an aluminium frame to hold a reflector at the bottom and an arm to hold a PV cell. The cell tilt can be varied from 0° to 90° relative to the zenith, i.e., horizontal to vertical cell, by rotating the arm about its own axis. The cell height can be varied from 4 to 12 cm by sliding the arm along the vertical aluminium post. The set-up was blackened to minimize stray reflection and slimmed to minimize shadows. For illuminating the cell, we used a solar simulator, which emits all the wavelengths of AM1.5G [see Fig. 3(b)], which represents the direct (i.e., unscattered) and diffuse solar irradiance received by a 37° tilted from the zenith, sun-facing surface under the US standard atmosphere, when the sun has a solar zenith angle of 48.2 [32] The outcoming beam was divergent in nature (half angle$<\pm$4°) and would cast a spot size of 16 cm on the ground [see Fig. 3(c)]. All the experiments were performed using a silicon heterojunction cell with an active area of 2 cm × 2 cm and total area of 4 cm × 4 cm [see Fig. 3(c)]. The following three types of measurements were performed for each sample, height, and tilt [see the schematic in Fig. 3(d)]: 1) output due to light entering the module through the front face ($J_{\mathrm{sc,F}}$); 2) output due to light entering the module through the rear face ($J_{\mathrm{sc,R}}$); and 3) output due to light entering the module through both faces ($J_{\mathrm{sc,F+R}}$). To get the output through one face, the other face was covered with black paper.

The relative error in the measurements was 5%. Further details and error analysis can be found in [33]. To simulate the experimental conditions, the spectral and angular dependent external quantum efficiency of the cell was calculated using PV Lighthouse SunSolve [34]. Details on the cell's properties can be found in [35] and [36]. Since 15% of the cell's active area is covered by the electrical contacts [see Fig. 3(c)], the calculated short-circuit current densities are multiplied by a factor of 0.85. The cell was illuminated with parallel beams of AM1.5G at normal incidence. [k_S, k_G, k_D] shown in Table I was used to emulate the reflectors. The surface roughness of m $= 0.2$ was given by the fits performed on the glossy lobe obtained from the goniometer [see Fig. 3(e)]. The resulting GGX-based glossy reflection function can be seen in Fig. 3(e).

We begin the discussion by analyzing the results for a mirror (see Fig. 4). The simulated $J_{\mathrm{sc,F}}$ [see Fig. 4(a)] shows dependence only on the cell tilt, which would be expected from a parallel beam. The measured $J_{\mathrm{sc,F}}$ [see Fig. 4(d)] also mainly depends on the cell tilt, but has a slight dependence on the height as well. This is caused by the diverging solar simulator beam, which leads to a higher intensity closer to the source. We find this behavior in all measurements. The simulated $J_{\mathrm{sc,R}}$ [see Fig. 4(b)] shows zero output since the normally incident parallel beam of rays is specularly reflected back in the vertical direction by the reflector while casting a shadow right underneath the

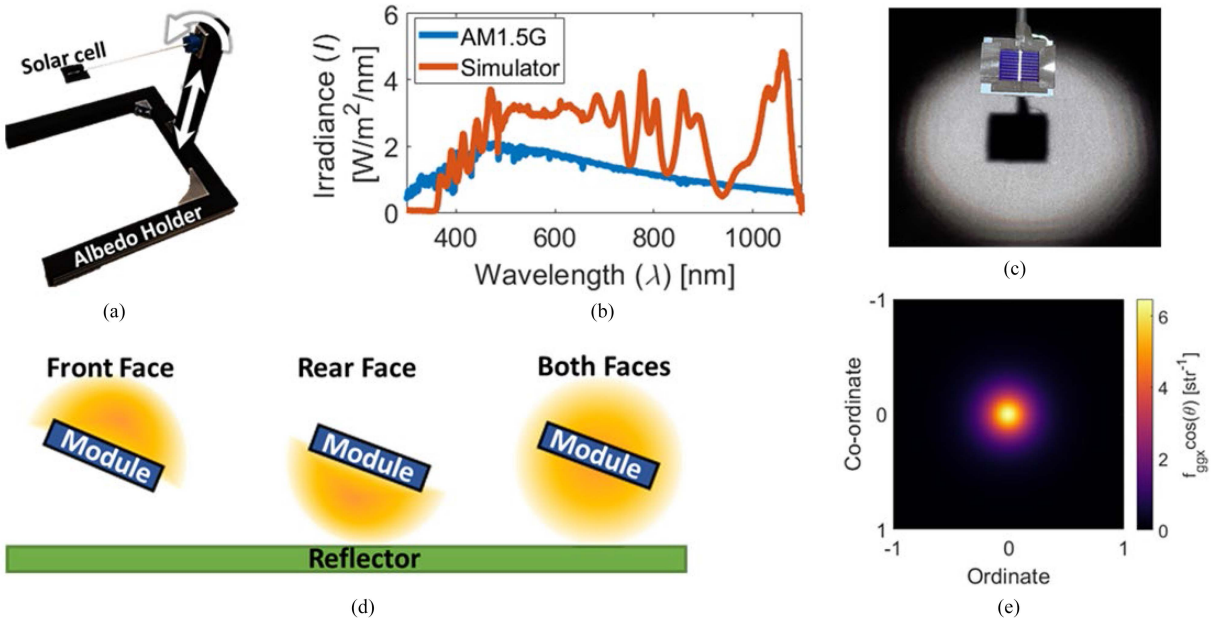

Fig. 3. Experimental set-up and validation. (a) Schematic of the experimental set-up. (b) Spectrum emitted by the solar simulator compared to the standard AM1.5G. (c) Photograph of the illuminated (spot size on the ground= 16 cm) silicon heterojunction bifacial cell (total area: 4 cm × 4 cm, active area: 2 cm × 2 cm) used. (d) Schematic of different types of illumination considered, namely, top, bottom, and total. (e) Reflection profile (top view) of a glossy material with m = 0.2 due to a normally incident light using GGX formalism.

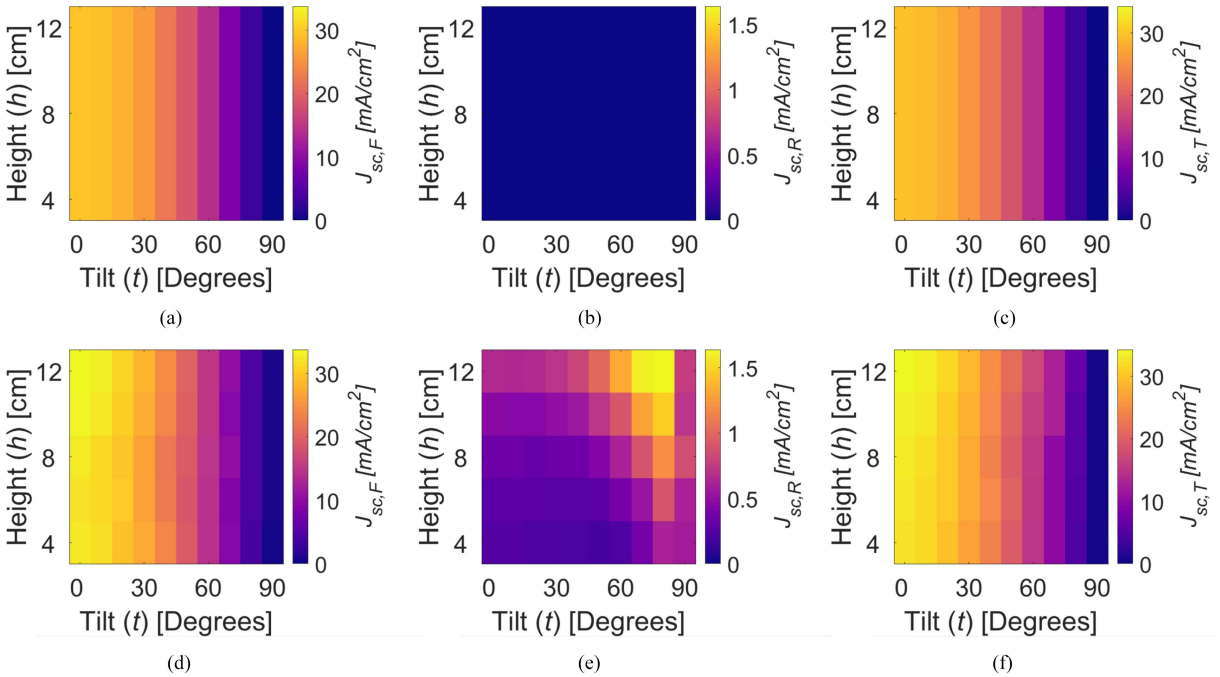

Fig. 4. Experimental validation for a mirror. (a) Simulated $J_{sc,F}$. (b) Simulated $J_{sc,R}$. (c) Simulated $J_{sc,T}$. (d) Measured $J_{sc,F}$. (e) Measured $J_{sc,R}$. (f) Measured $J_{sc,T}$. The subscripts F, R, T stand for front face, rear face, and total, respectively.

cell. Thereby, for a perfectly parallel beam the contribution of the specular reflector is zero. Since the beam in the experiments is slightly divergent, we did obtain some contribution on the rear side from reflection [see Fig. 4(e)]. Simulated $J_{sc,T}$ [see Fig. 4(c)] displays a behavior identical to that of $J_{sc,F}$, since $J_{sc,R}$ is zero, as $J_{sc,T} = J_{sc,F} + J_{sc,R}$. Again, because of the slight beam divergence, in the experiment $J_{sc,T}$ is a bit increased for high tilt and height compared to $J_{sc,F}$ [see Fig. 4(f)].

For simulated $J_{sc,F}$ with photopaper and paper (see Figs. 5(a) and 6(a), respectively), we see a slightly different output as was observed for the mirror [see Fig. 4(a)]. A higher output is seen in the region of lower height and higher tilt for photopaper

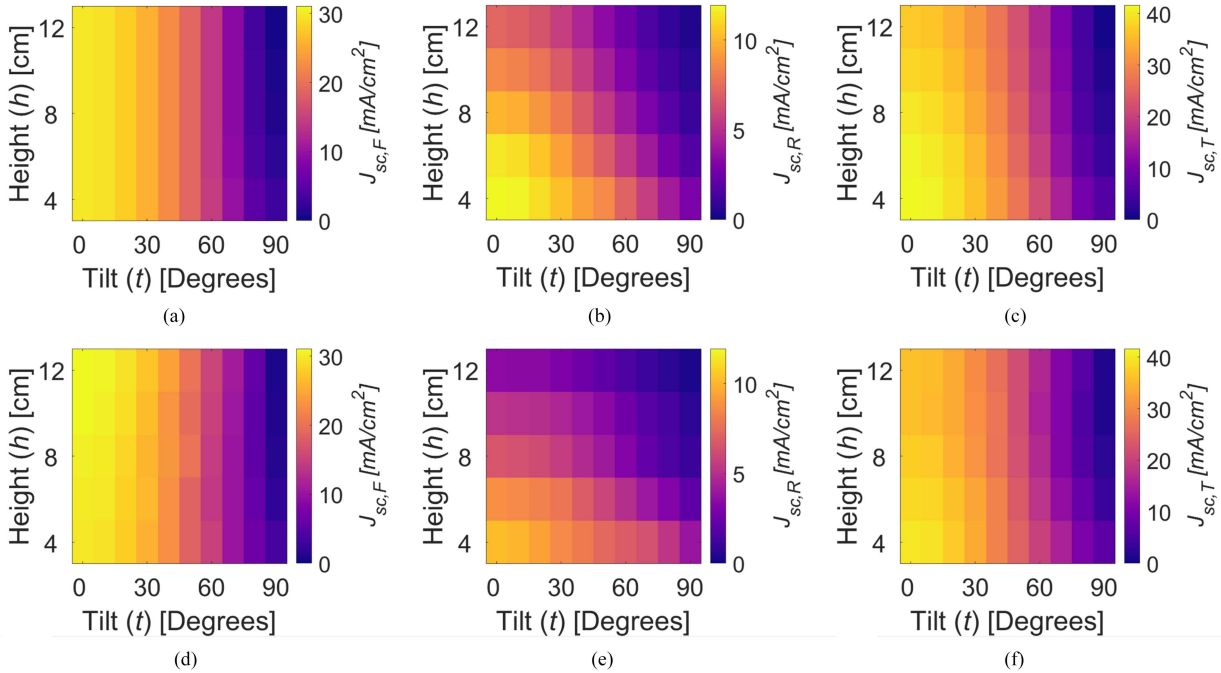

Fig. 5. Experimental validation for photopaper. (a) Simulated $J_{\mathrm{sc,F}}$. (b) Simulated $J_{\mathrm{sc,R}}$. (c) Simulated $J_{\mathrm{sc,T}}$. (d) Measured $J_{\mathrm{sc,F}}$. (e) Measured $J_{\mathrm{sc,R}}$. (f) Measured $J_{\mathrm{sc,T}}$. The subscripts F, R, T stand for front face, rear face, and total face, respectively.

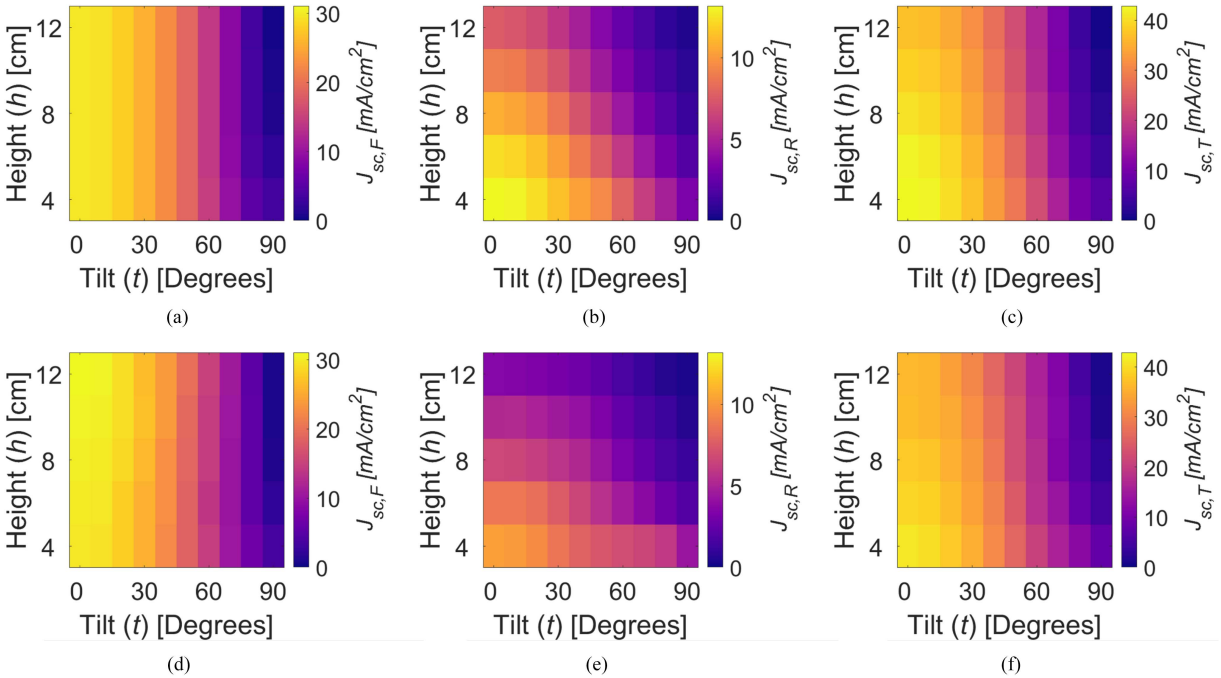

Fig. 6. Experimental validation for paper. (a) Simulated $J_{\mathrm{sc,F}}$. (b) Simulated $J_{\mathrm{sc,R}}$. (c) Simulated $J_{\mathrm{sc,T}}$. (d) Measured $J_{\mathrm{sc,F}}$. (e) Measured $J_{\mathrm{sc,R}}$. (f) Measured $J_{\mathrm{sc,T}}$. The subscripts F, R, T stand for front face, rear face, and total face, respectively.

and paper. This is because as the diffusiveness of the reflector increases, more light can be redirected to the front face of the cell. At lower height, the cell is the closest to the reflector, and hence, can capture more. For greater tilt, the shadow is minimal, which leads to more light being incident on the cell. For simulated $J_{\mathrm{sc,R}}$ for photopaper and paper [as shown in Figs. 5(b) and 6(b)], we see a maximum for lower height and lower tilt. This is because as the cell moves further away from the reflector, more reflected light is lost in directions away from the cell, as the reflection is now over a wider lobe. Furthermore, as the module tilt increases, the rear face's exposure to the reflector reduces, which leads to a lower rear output. Finally, for the simulated $J_{\mathrm{sc,T}}$ due to the photopaper and paper [see Figs. 5(c) and 6(c)], we see the cumulative effect of the respective $J_{\mathrm{sc,F}}$ and $J_{\mathrm{sc,R}}$.

TABLE II
NRMSE FOR THE SAMPLES

Sample	NRMSE		
	$J_{sc,F}$	$J_{sc,R}$	$J_{sc,T}$
Mirror	0.39	0.49	0.60
Photopaper	0.22	0.30	0.29
Paper	0.19	0.30	0.28

The agreement between the simulated and measured data is quantified in terms of normalized root-mean-square error (NRMSE), which is given as

$$\text{NRMSE} = \sqrt{\frac{\sum_{i=1}^{n}(s_i - m_i)^2}{\text{n}}} / \left(\max(m_i) - \min(m_i)\right) \tag{6}$$

where s_i and m_i are simulated and measured quantities, and n is the total number of the configurations. Here, $n = 50$, denoting 5 different heights and 10 different cell tilts.

The NRMSE, is given in Table II for all cases. For the measured $J_{\text{sc,F}}$ [see Figs. 4(d), 5(d), 6(d)], we notice a maxima for higher height and lower tilt. This is because as the height increases, the cell moves closer to the source. Since the source is diverging, the closer the cell is to the source, the higher is the intensity. This effect is strongest for a horizontal cell as it is the most exposed to the source above. As the tilt increases, this effect decreases due to reduced exposure. For measured $J_{\text{sc,R}}$ due to a mirror [see Fig. 4(e)], we see some output as opposed to the simulated $J_{\text{sc,R}}$ [see Fig. 4(b)]. This is because of the diverging incoming beam and stray radiation, further exaggerated by the nonideal specularity of the reflector. The agreement between simulated and measured data can be improved by: 1) accounting for the divergence of the incoming source and simulating for those angles of incidence; 2) using an even better collimated source of uniform illumination to reduce stray radiation; and 3) simulating more realistic spectral and angular properties of the cell that match the real cell better.

Overall, we also see good quantitative agreement between simulations and experiments, thus proving the mettle of the methodology presented here.

V. PV Performance Due to Ideal Specular and Diffuse Albedo

In the previous sections, we demonstrated how our ray tracing model accounts for the angle dependence and BRDF of different materials and validated this framework experimentally. In this section, we will use our validated model to determine the upper limit or the maximum potential for PV enhancement. This can be brought about by ideal reflectors. Ideal reflectors reflect 100% of light, i.e., without any loss. Ideal specular and diffuse reflectors are characterized by $k_S = 1$ and $k_D = 1$, respectively.

A. Short-Circuit Current Density

We use the previously mentioned software to calculate and analyze the performance of a free-standing, south-facing silicon heterojunction bifacial module as a function of time of the day (T) and module tilt (t). A 1 m $\times$ 1.5 m module located at a height of 1 m from the ground and a reflector size of 10 m $\times$ 15 m was assumed. The module normal or tilt was varied from 0° to 90°, i.e., horizontal to vertical, relative to the zenith. The incident spectrum used is the standard AM1.5G [see Fig. 3(b)]. The location and date for the study was fixed to be Enschede (52.2°, 6.8°), The Netherlands, and 6/22/2022, respectively. The corresponding solar position in terms of solar zenith (θ_{sol}) and solar azimuth (ϕ_{sol}) from sunrise to sunset is shown in Fig. 7(a). The region bounded inside the vertical dashed lines show the time frame for which the sun is in the south. The north is represented by $\phi_{sol} = 0°$, increasing east-ward. With all the parameters defined, we first calculate the module's short-circuit current density. Namely: 1) $J_{\text{sc,top}}$ for light received from the sky or the sun, i.e., usually the top [see Fig. 7(b)]; 2) $J_{\text{sc,front}}$ for light received from the bottom or the reflector through the module's front face [see Fig. 7(c) and (d)]; and 3) $J_{\text{sc,rear}}$ for light received from the bottom or the reflector through the module's rear face [see Fig. 7(e) and (f)].

In Fig. 7(b), we examine $J_{\text{sc,top}}$ as a function of the sun's position, given in terms of time of the day, and module tilt. The maximum for any given tilt always occurs around solar noon ($T \sim 13:34$ h), when the sun has the highest position in the sky. Overall, a 30° tilted module leads to the highest output as it best oriented with respect to the varying sun's position. In particular, it's perpendicular to the irradiance at solar noon. During the early and late hours, the sun is in the north and occupies shallow zenith positions [see Fig. 7(a)]. This leads to a lower output, in general, as the angle of incidence is poor. For slightly larger zenith, the sun's azimuth moves towards the edge of the module. At these angles, the incoming rays are closer to the modules' horizontal, where the conversion efficiency is low [36]. Hence, a region of low output occurs. Note that the output at high tilt and high zenith [so upper left and right corner in Fig. 7(b)] originates from the rear face of the bifacial module, whereas in all other situations, the irradiance is received from the front. Fig. 7(c) and (d) shows $J_{\text{sc,front}}$, the output due to the light reflected onto the front face of the module, by an ideal specular and diffuse albedo, respectively. For both reflectors, the output increases as the module tilt increases because the front face gets more exposed to the reflector. As a consequence, $J_{\text{sc,front}}$ reaches a maximum at $t = 90°$ for both the reflectors. The $J_{\text{sc,front}}$ drops to zero for all the reflectors for $t < 16.7°$, as the front face is no more exposed to the reflector. For a specular reflector [see Fig. 7(c)], the output for $T < 09:00$ and $T > 18:30$ is zero. This is because the sun is in the north, i.e., on the module backside [shown by dashed line in Fig. 7(a)]. Hence, the reflected rays hit only the back of the module. The output reaches a maximum around solar noon. For a diffuse reflector [see Fig. 7(d)], the changes in output are more gradual. This is due to the fact that a diffuse reflector reflects over the entire upper hemisphere, thus leading to a more homogeneous illumination.

Fig. 7(e) and (f) shows $J_{\text{sc,rear}}$ the output due to the light reflected on the rear face of the module, by an ideal specular and diffuse albedo, respectively. For both the reflectors, when the sun is in the south, the highest yield occurs for $t = 0°$, i.e., a horizontal module, as it ensures maximum exposure to the reflector. For a specular reflector [see Fig. 7(e)], around sunrise

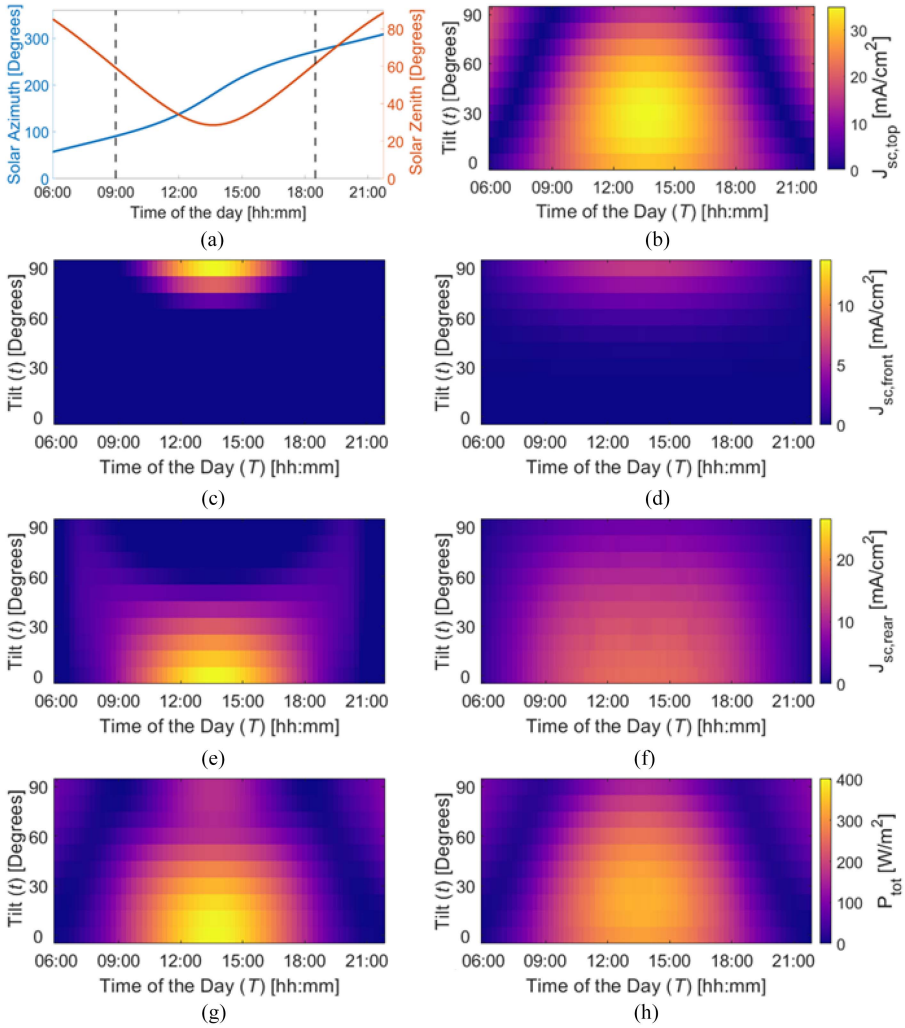

Fig. 7. Computationally simulated output for ideal reflectors. (a) Solar path in terms of solar zenith and solar azimuth for Enschede, The Netherlands for 6/22/2022. The region marked within the dashed vertical lines show the time when the sun is in the south. (b) Short-circuit current-density due to AM 1.5G emanating from the sky or top ($J_{\text{sc,top}}$). (c), (d) Albedo-dependent short-circuit current-density generated by irradiance onto the front face of the module ($J_{\text{sc,front}}$) due to a specular and diffuse albedo, respectively. (e), (f) Albedo-dependent short-circuit current-density generated by irradiance onto rear face of the module ($J_{\text{sc,rear}}$) due to a specular and diffuse albedo, respectively. (g), (h) Total power per unit area (P_{tot}) with a specular and diffuse albedo, respectively.

and sunset, the angle of reflection is such that the specularly reflected rays never hit the module, given the geometry at hand. This changes as the day progresses or the solar position changes. For $t > 60^\circ$, as the sun's elevation angle increases, the rays are reflected at such an angle that they hit the front of the module. This leads to an output from the front face [see Fig. 7(d)], instead of the rear and causes a dark semicircle-like region for $t > 60^\circ$, the inverse of which can be found in Fig. 7(d). For a diffuse reflector [see Fig. 7(f)], again, the variation in output is more gradual as it reflects over the entire hemisphere.

B. Power Per Unit Area

The instantaneous power per unit area (P) due to a reflector-module is calculated using

$$P = FF.V_{\text{oc}}.\ J_{\text{tot}} \tag{7}$$

$$\text{such that} \quad V_{\text{OC}} = \frac{k_{\text{B}}T_{\text{mod}}}{q} \ln\left(\frac{J_{\text{l}}}{J_{\text{d}}} + 1\right) \tag{8}$$

$$J_{\text{sc,tot}} = J_{\text{sc,front}} + J_{\text{sc,rear}} + J_{\text{sc,top}} \tag{9}$$

where FF is the fill factor or the "squareness" of the I-V curve of the module, and was assumed to be 0.85 for this study. V_{oc} is the open-circuit voltage or the highest voltage that can be generated by a module. k_{B} is the Boltzmann constant, T_{mod} is the module temperature, J_{l} is the light generated current-density, and J_{d} is the dark saturation current density. Here, $J_d = 2.44\,\text{mA}/\text{cm}^2$.

The resulting power plots for specular and diffuse are shown in Fig. 7(g) and (h) is a combination of $J_{\text{sc,top}}$ [see Fig. 7(b)] and their respective $J_{\text{sc,front}}$ and $J_{\text{sc,rear}}$ [see Fig. 7(c) and (d)]. The highest output occurs due to a specular reflector at $t = 0^\circ$ for the given day and location, ($\sim$9% more than a diffuse reflector).

A good reflector is not only supposed to redirect more light but is also supposed to be more robust to the change in the solar position. This makes a diffuse reflector an overall winner.

C. Mismatch

Another important aspect of solar power production is the module mismatch. A solar module consists of many photovoltaic

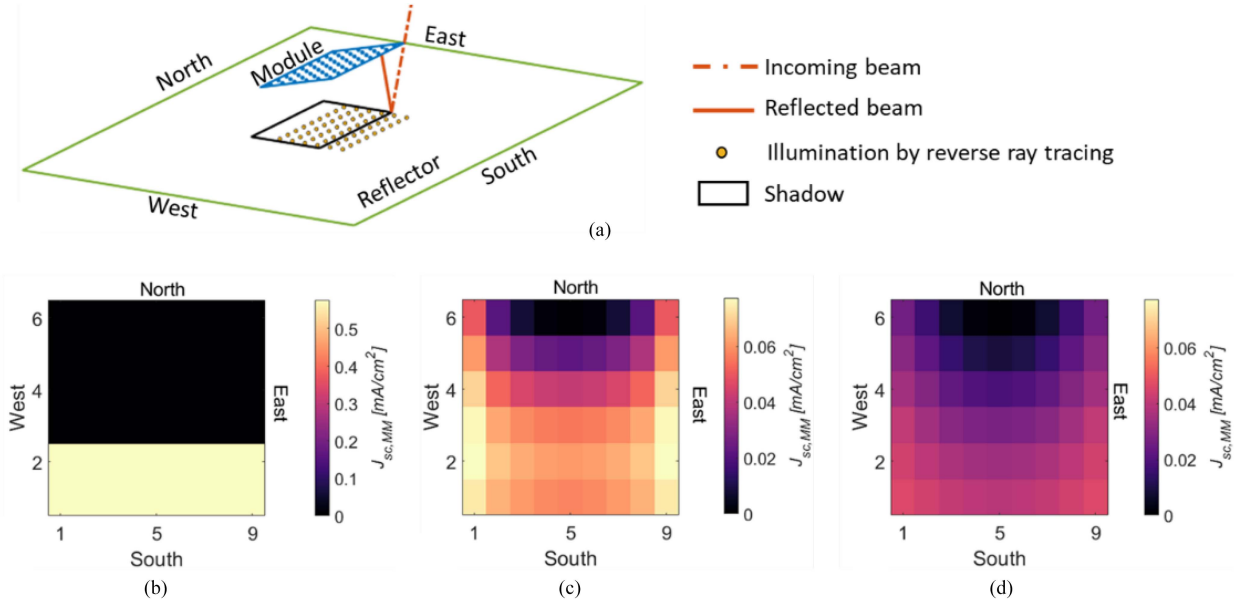

Fig. 8. Mismatch due to reflectors. (a) Schematic of the configuration assumed. Mismatch induced due to (b) specular, (c) glossy, and (d) diffuse reflector, respectively.

cells electrically connected, at least partially in series. Any spatial inhomogeneity in the incident illumination on the module leads to spatially varying short-circuit current density within the module, i.e., not all cells produce the equal short-circuit current density. Thus, due to series current matching condition, the short-circuit current of a string is limited by the lowest value. The difference in the short-circuit current density between highest and lowest output ($J_{\mathrm{sc,\ MM}}$) is given out as heat (i.e., loss) and can damage the cell. Thus, while discussing the merit of a ground-reflector, the module mismatch introduced by it must also be considered. For this work, we quantify the mismatch as the difference between the J_{sc} at a given point on the module and the minimum J_{sc} on the module.

A south-facing 30° tilted module (1 m × 1.5 m) was fixed at a height of 1.5 m from the reflector (10 m × 15 m). AM1.5G was made incident at $[\theta_{sol}, \phi_{sol}] = [5°, 180°]$. The schematic is shown in Fig. 8(a). Fig. 8(b)–(d) shows mismatch across a module due to a specular, glossy (m = 0.4), and a diffuse reflector, respectively. Note, the color bar for specular is different to that of glossy and diffuse due to vastly different values. In the schematic [see Fig. 8(a)], the black rectangle shows the shadow cast by the module, and the yellow dots show the illuminated spots due to the reverse ray-tracing from the module pixels. Only the illuminated spots outside the shadow contribute light for output generation in the module. As a consequence of this, we see a higher output in the southern-side of the module [see Fig. 8(b)–(d)]. This effect is the strongest for a specular reflector, and gradually alleviates as one moves towards diffuse. This is because of the widening of the reflection lobe. Another consequence of the wider lobe can be seen at the east and west edges. As the reflection lobe widens, more light is spread out across the module through the east and west edges. This leads to the diffuse reflector inducing the least mismatch.

Such an analysis of mismatch can not only help in developing better albedos that can enhance the yield but also prevent mismatch-related damages to a PV module.

VI. Conclusion

We present a comprehensive method to describe and lay rules for designing a good reflector for PV yield enhancement. Ignoring spectral and angular composition of the incoming and ground-reflected irradiance can lead to errors in power and LCOE estimations as high ∼24% and ∼65%, respectively. Therefore, we developed an experimentally validated framework to successfully characterize spectro-angular reflectance of wide range of materials (i.e., mirror-specular, paper-diffuse, photopaper-glossy, and diffuse). We determined the k coefficients for generic paper, photopaper, and mirror. These coefficients, along with a reverse ray-tracing software enabled us to simulate the influence of these diverse reflectors on solar power generation under realistic conditions, i.e., for any illumination, height, and tilt. Our analysis clearly demonstrates the need for a more nuanced discussion for benchmarking and designing albedo materials. From an optics-perspective, a good reflector must: 1) redirect more light onto the module; 2) redirect light as homogeneously as possible, i.e., reduce mismatch; and 3) be robust to the changing sun's position.

The abovementioned calculations can be expanded to include solar tracking systems, local spectro-angular irradiance data, and thermal variations. This approach provides a rigorous framework for analyzing a bifacial power plant performance due to any ground-reflector. When used with an optimization algorithm for yield enhancement or machine-learning algorithm, it can help design and optimize novel or exotic reflectors like free-space luminescent solar concentrators [22] and metamaterial-based

reflectors [21]. Such a knowledge of the properties of a reflector can serve as the "target" solution and streamline the quest for better reflectors.

ACKNOWLEDGMENT

The authors would like to thank A. Mahmoudi, M. Mehrali, and W. Sultanpoor for helping with the solar simulator and A. Augusto for providing bifacial solar cells, like to thank J. Y. Zheng for providing schematics shown in Fig. 1(b)–(d), like to thank S. Ovaitt and M. A. Alam for their invaluable feedback on the manuscript, and also like to thank L. Horst and A. Rikhof for troubleshooting the code and helpful discussions.

Author Contribution: S. S Pal and R. Saive conceived the project. The goniometer measurements were performed by J. Westerhof, and the UV-VIS measurements were performed by S. S Pal. F. van Loenhout and S. S Pal performed the measurements and analysis for experimental validation. The reverse ray tracing simulations were designed and performed by S. S Pal. S. S Pal wrote the original draft, and all the authors edited the manuscript. R. Saive supervised the project.

REFERENCES

[1] R. Eriksen et al., "Energy transition outlook 2021: Technology progress report," 2021.
[2] J. B. Jahangir et al., "A critical analysis of bifacial solar farm configurations: Theory and experiments," *IEEE Access*, vol. 10, pp. 47726–47740, 2022.
[3] M. H. Riaz, H. Imran, R. Younas, and N. Z. Butt, "The optimization of vertical bifacial photovoltaic farms for efficient agrivoltaic systems," *Sol. Energy*, vol. 230, pp. 1004–1012, 2021.
[4] M. H. Riaz, H. Imran, H. Alam, M. A. Alam, and N. Z. Butt, "Crop-specific optimization of bifacial PV arrays for agrivoltaic food-energy production: The light-productivity-factor approach," *IEEE J. Photovolt.*, vol. 12, no. 2, pp. 572–580, Mar. 2022.
[5] P. E. Campana, B. Stridh, S. Amaducci, and M. Colauzzi, "Optimisation of vertically mounted agrivoltaic systems," *J. Cleaner Prod.*, vol. 325, 2021, Art. no. 129091.
[6] "International technology roadmap for photovoltaic (ITRPV)," Verband Deutscher Maschinen- und Anlagenbau (VDMA), 2022.
[7] X. Sun, M. R. Khan, C. Deline, and M. A. Alam, "Optimization and performance of bifacial solar modules: A global perspective," *Appl. Energy*, vol. 212, pp. 1601–1610, 2018.
[8] A. Cuevas, A. Luque, J. Eguren, and J. D. Alamo, "50 per cent more output power from an albedo-collecting flat panel using bifacial solar cells," *Sol. Energy*, vol. 29, no. 5, pp. 419–420, 1982.
[9] M. Brennan, A. Abramase, R. Andrews, and J. Pearce, "Effects of spectral albedo on solar photovoltaic devices," *Sol. Energy Mater. Sol. Cells*, vol. 124, pp. 111–116, 2014.
[10] T. C. R. Russell, R. Saive, and H. A. Atwater, "Thermodynamic efficiency limit of bifacial solar cells for various spectral albedos," in *Proc. IEEE 44th Photovolt. Specialist Conf.*, 2017, pp. 1531–1536.
[11] T. C. R. Russell, R. Saive, A. Augusto, S. G. Bowden, and H. A. Atwater, "The influence of spectral albedo on bifacial solar cells: A theoretical and experimental study," *IEEE J. Photovolt.*, vol. 7, no. 6, pp. 1611–1618, Nov. 2017.
[12] R. Gottschalg, T. Betts, D. Infield, and M. J. Kearney, "The effect of spectral variations on the performance parameters of single and double junction amorphous silicon solar cells," *Sol. Energy Mater. Sol. Cells*, vol. 85, no. 3, pp. 415–428, 2005.
[13] P. Faine, S. R. Kurtz, C. Riordan, and J. M. Olson, "The influence of spectral solar irradiance variations on the performance of selected single-junction and multijunction solar cells," *Sol. Cells*, vol. 31, no. 3, pp. 259–278, 1991.
[14] J. Balenzategui and F. Chenlo, "Measurement and analysis of angular response of bare and encapsulated silicon solar cells," *Sol. Energy Mater. Sol. Cells*, vol. 86, no. 1, pp. 53–83, 2005.
[15] M. T. Patel et al., "Temperature dependent energy gain of bifacial PV farms: A global perspective," *Appl. Energy*, vol. 276, 2020, Art. no. 115405.
[16] M. R. Khan, E. Sakr, X. Sun, P. Bermel, and M. A. Alam, "Ground sculpting to enhance energy yield of vertical bifacial solar farms," *Appl. Energy*, vol. 241, pp. 592–598, 2019.
[17] K. McIntosh, M. Abbott, and B. Sudbury, "SunSolve Yield," PV Lighthouse. Accessed: Jun. 22, 2022. [Online]. Available: https://www.pvlighthouse.com.au/sunsolve-yield
[18] "PVSyst." Accessed: Jun. 22, 2022. [Online]. Available: https://www.pvsyst.com/
[19] "PVcase," IMEC. Accessed: Jun. 22, 2022. [Online]. Available: https://pvcase.com/yield/
[20] S. Pal, *Tracing the Light: Designing Reflectors for Bifacial Photovoltaic Yield Enhancement Under Outdoor Irradiance*. Enschede, The Netherlands: Univ. of Twente, 2022.
[21] B. Slovick, Z. G. Yu, M. Berding, and S. Krishnamurthy, "Perfect dielectric-metamaterial reflector," *Phys. Rev. B*, vol. 88, Oct. 2013, Art. no. 165116.
[22] G. Heres, L. Einhaus, and R. Saive, "Analytical model for the performance of a free-space luminescent solar concentrator," in *Proc. IEEE 48th Photovolt. Specialists Conf.*, 2021, pp. 1027–1029.
[23] L. Einhaus and R. Saive, "Free-space concentration of diffused light for photovoltaics," in *Proc. IEEE 47th Photovolt. Specialists Conf.*, 2020, pp. 1368–1370.
[24] S. A. Pelaez et al., "Holographic cap collectors for enhanced mid-day energy production of vertically mounted bifacial photovoltaic modules," *Nonimaging Opt., Efficient Des. Illumination Sol. Concentration XV*, SPIE, vol. 10758, pp. 143–153, 2018.
[25] F. E. Nicodemus, "Directional reflectance and emissivity of an opaque surface," *Appl. Opt.*, vol. 4, no. 7, pp. 767–775, 1965.
[26] B. Walter, S. R. Marschner, H. Li, and K. E. Torrance, "Microfacet models for refraction through rough surfaces," in *Proc. 18th Eurographics Conf. Rendering Techn.*, 2007, pp. 195–206.
[27] "6080 white reflectance coating-product code: AA-005XX-000," Labsphere. Accessed: Jun. 30, 2022. [Online]. Available: https://www.labspherestore.com/product-p/aa-005xx-000.htm
[28] C. J. Bruegge et al., "Reflectance stability analysis of Spectralon diffuse calibration panels," in *Proc. SPIE Calibration Passive Remote Observing Opt. Microw. Instrum.*, 1991, vol. 1493, pp. 132–142.
[29] "Perkin Elmer." Accessed: Jun. 22, 2022. [Online]. Available: https://resources.perkinelmer.com/corporate/cmsresources/images/44-74450bro_lambda8509501050.pdf
[30] O. Hrytsenko, V. Shvalagin, G. Grodziuk, and V. Granchak, "Influence of parameters of screen printing on photoluminescence properties of nanophotonic labels for smart packaging," *J. Nanotechnol.*, vol. 2017, 2017, Art. no. 7125682.
[31] J. Westerhof, *Investigation of Spectro-Angular Albedo of Diffuse, Glossy, and Specular Surfaces for Enhanced Photovoltaic Output*. Enschede, The Netherlands: Univ. of Twente, 2021.
[32] *Standard Tables for Terrestrial Direct Normal Solar Spectral Irradiance for Air Mass 1.5*, ASTM E891, 87th Ed., 1992.
[33] F. V. Loenhout, *Influence of Albedo on Bifacial Solar Module Output: An Experimental Approach*. Enschede, The Netherlands: Univ. of Twente, 2021.
[34] PV LightHouse: SunSolve. [Online]. Available: https://www.pvlighthouse.com.au/
[35] R. Saive, T. C. R. Russell, and H. A. Atwater, "Enhancing the power output of bifacial solar modules by applying effectively transparent contacts (ETCs) with light trapping," *IEEE J. Photovolt.*, vol. 8, no. 5, pp. 1183–1189, Sep. 2018.
[36] S. Pal, A. Reinders, and R. Saive, "Simulation of bifacial and monofacial silicon solar cell short-circuit current density under measured spectro-angular solar irradiance," *IEEE J. Photovolt.*, vol. 10, no. 6, pp. 1803–1815, Nov. 2020.